Photocatalytic H_2-production and benzyl-alcohol-oxidation mechanism over CdS using Co^{2+} as hole cocatalyst

Xianglin Xiang [a], Bicheng Zhu [b], Jianjun Zhang [b], Chenhui Jiang [c], Tao Chen [c], Huogen Yu [b], Jiaguo Yu [a,b,*], Linxi Wang [b,**]

[a] *State Key Laboratory of Advanced Technology for Materials Synthesis and Processing, Wuhan University of Technology, Wuhan 430070, PR China*
[b] *Laboratory of Solar Fuel, Faculty of Materials Science and Chemistry, China University of Geosciences, Wuhan 430074, PR China*
[c] *Hefei National Laboratory for Physical Sciences at Microscale, CAS Key Laboratory of Materials for Energy Conversion, Department of Materials Science and Engineering, University of Science and Technology of China, Hefei, Anhui 230026, PR China*

ARTICLE INFO	ABSTRACT
	The sluggish oxygen evolution reaction (OER) is often the bottleneck of photocatalytic overall water splitting, greatly suppressing the hydrogen-production activity. Herein, the slow OER was replaced by selective benzyl alcohol (BA) oxidation to benzaldehyde (BD) to promote H_2 production. The photocatalytic reaction was conducted over CdS quantum dots, which were modified with Co^{2+} hole cocatalysts to further accelerate the rate-limiting BA oxidation. The photocatalytic system exhibits an ultra-high H_2-production rate of 257.8 mmol g^{-1} h^{-1} with a remarkable apparent quantum yield of 69.3% under 365-nm light irradiation. The high performance is attributed to the Co^{2+} hole cocatalysts on CdS surfaces, which not only enhance light absorption but also facilitate photogenerated carrier transfer. More importantly, both photogenerated electrons and holes are fully utilized in meaningful reactions. This work exemplifies a bifunctional photocatalytic system for simultaneous production of self-separated hydrogen and benzaldehyde, both of which are important industrial products.

1. Introduction

Photocatalytic water splitting is a promising approach to harness solar energy to produce clean hydrogen energy [1–3]. The process of overall water splitting consists of hydrogen evolution reaction (HER) and oxygen evolution reaction (OER), which are induced by photogenerated electrons and holes, respectively. However, due to low efficiency, poor stability, high cost, and the difficulty in separating the gaseous hydrogen and oxygen products, this technology is still at infancy. In practice, OER is an ultraslow four-electron process, which is the bottleneck of overall water splitting and greatly limits the photocatalytic performance [4]. Plus, oxygen has a low economic value and may cause photocorrosion [5]. As a result, sacrificial reagents are utilized to consume photogenerated holes to avoid OER. However, this strategy is not economically feasible due to the consumption of valuable chemicals (e.g., ethanol [6], lactic acid [7], glycerol [8], triethanolamine [9], etc.). Instead, it is more desired to couple HER with profitable oxidation reactions. As a common aromatic aldehyde, benzaldehyde

(BD) is wildly used as an important raw material for the pharmaceutical industry or as an additive in plastic manufacturing [10–12]. BD can be prepared via the partial oxidation of toluene, the hydrolysis of benzyl chloride, or the selective oxidation of benzyl alcohol (BA) [13]. Among them, the latter approach stands out due to high BD yields and product selectivity [14,15]. However, this process operates under high temperatures and uses precious metal catalysts and hazardous organic solvents, resulting in massive energy consumption and environmental pollution [16]. Therefore, it is more desirable to execute this reaction under milder and greener conditions. A promising solution is to construct a photocatalytic system to couple hydrogen evolution with oxidation of BA to BD [17,18]. In this system, photogenerated electrons reduce H^+ to H_2, and photogenerated holes oxidize BA to BD [19]. The advantages of this tactic include: (1) substituting the slow four-electron OER with the oxidation of BA to BD, which is a more kinetically feasible two-electron reaction; (2) significantly inhibiting back-reactions owing to the self-separation of gaseous H_2 and liquid BD; (3) suppressing photocorrosion caused by O_2; (4) avoiding the usage of sacrificial agents while

producing valuable BD. Thus, this process holds great promise to boost H_2-evolution activity and efficiently utilize photogenerated holes.

Recently, quantum dots (QDs) have attracted tremendous attention for their superb light-harvesting properties, abundant surface sites, facile carrier separation, and tunable band gaps [20,21]. Due to the small particle size of QDs, photogenerated carriers can easily transfer to the surfaces, resulting in efficient carrier transfer. Because of the quantum confinement effect, the band gaps of QDs can be precisely controlled by varying the particle size [22]. However, the photocatalytic performance of QDs is limited by rapid recombination of photogenerated charge carriers and insufficient active sites. Therefore, cocatalysts are employed to promote the separation of photogenerated carriers and create active sites for surface redox reactions [23]. Various electron cocatalysts such as Pt [24,25], Ni [26], MoS_2 [27,28], and Co_2C [29], etc., have been wildly used in photocatalytic hydrogen evolution systems. However, the oxidation reaction is still slow and more robust cocatalysts are in need.

Metal ions have been gradually developed as cocatalysts since they can be easily loaded on photocatalysts and form intimate interfacial contact through electrostatic attraction [30]. Previously, we have successfully introduced Mn^{n+} ions to improve the photocatalytic CO_2 reduction performance of ZnO [31]. The Mn^{n+} ions with switchable valence states can capture photogenerated electrons on the CB of ZnO and provide the electrons for CO_2 reduction. Motivated by the unique properties of QDs and metal ion cocatalysts, we herein report the integration of CdS QD with Co^{2+} as hole cocatalysts to simultaneously realize high-performance photocatalytic H_2 production and selective oxidation of BA into BD. This photocatalytic system presents an ultra-high H_2-production rate of 257.8 mmol g^{-1} h^{-1} with an apparent quantum yield of 69.3% under 365 nm light irradiation. The H_2-production rate is the highest among all reported photocatalysts to the best of our knowledge (Table S1). Furthermore, BA conversion of 83.9% with BD selectivity of 77.6% is achieved after photoreaction for 3 h. Isotope tracing proves that H_2 mainly derives from water. Femtosecond transient absorption (fs-TA) spectra reveal that CoS in-situ formed on the surface of CdS QDs during the photodeposition of Co^{2+} mainly functions as a hole cocatalyst. In addition, density functional theory (DFT) calculations illustrate the reaction pathway of selective BA conversion to BD. A photocatalytic mechanism is speculated to explain the effect of CoS modification leads on enhancing photocatalytic performance.

2. Experimental section

2.1. Materials

CdO, NaOH, *n*-hexane, and methanol were bought from Sinopharm Chemical Reagent Co., Ltd. The other chemical reagents were purchased from Aladdin and used as received without further purification.

2.2. Materials synthesis

2.2.1. The synthesis of oil-soluble CdS QDs (CdS-O)

The CdS-O was synthesized via a solvent-thermal method [32]. Typically, a solution containing 4 mmol of CdO, 8 mL of oleic acid (OA), and 8 mL of 1-octadecene (ODE) was heated to 230 ℃ in an N_2 atmosphere to form a Cd-precursor solution. Subsequently, sulfur powders (4 mmol) were dissolved into 5 mL of oleylamine (OAm) to form the S-OAm solution, which was added to the Cd precursor to form CdS-O. The prepared CdS-O was re-dispersed in 20 mL of *n*-hexane for further use.

2.2.2. The synthesis of water-soluble CdS QDs (CdS-W)

The synthesized CdS-O was transformed into CdS-W by replacing the initial hydrophobic surfactants (OA and/or OAm) with hydrophilic mercaptopropionic acids (MPA) following previous literature [33]. Firstly, 0.5 mL of MPA was added to 5 mL of methanol. Subsequently, a

NaOH solution (40 wt%) was added into the solution dropwise to adjust the pH to 13. The solution was added to 20 mL of the CdS-O sample and stirred for 3 h. Finally, the CdS-W was collected by precipitating the QDs by adding excess acetone antisolvent. The final products were washed with acetone and water 3 times each and re-dispersed into water.

2.2.3. The synthesis of cobalt hybrid water-soluble CdS QDs (Co-CdS-W)

The Co-CdS-W were prepared through a direct photoinduced deposition process in the presence of $CoCl_2 \cdot 6$ H_2O (1.6 mM) and light illumination.

The detailed methods for characterization, photocatalytic H_2 production test, and computational calculations are given in the Supporting Information.

3. Results and discussion

3.1. Morphology and structure

As shown in Fig. 1a, the preparation of cobalt hybrid water-soluble CdS QDs (Co-CdS-W) involves three steps. The oil-soluble CdS QDs (CdS-O) was firstly prepared via a solvothermal method. Then, the as-prepared CdS-O was transformed into water-soluble CdS QDs (CdS-W) via ligand exchange with MPA as the capping reagent. Finally, Co-CdS-W was prepared through direct photoinduced deposition in the presence of $CoCl_2 \cdot 6$ H_2O.

The structural and chemical properties of the prepared samples were characterized by X-ray diffraction (XRD), Fourier transform-infrared (FT-IR) spectroscopy, Raman spectra, and Zeta potential measurements. XRD measurements were employed to determine the crystalline structure of CdS-O, CdS-W, and Co-CdS-W. As shown in Fig. 1b, all samples present three main peaks at 26.5°, 44.0°, and 52.1°, corresponding to (111), (220), and (331) facets of cubic CdS (joint committee on powder diffraction standards, JCPDS No. 75–0581), respectively. Compared to the XRD pattern of CdS-O, no extra peaks are observed in that of CdS-W, indicating that the crystal structure of CdS-W remain unchanged during ligand exchange. No diffraction peaks of Co compounds (CoS, $Co(OH)_2$, or CoO) were detected in Co-CdS-W, which was attributed to their low contents. The XRD peaks of CdS-W and Co-CdS-W are at the same positions, revealing that Co species mainly existed on the surface of CdS-W rather than penetrating into CdS lattices. The large peak widths imply the small crystalline size of CdS particles [34]. FT-IR measurements were employed to investigate the functional groups on the prepared samples and the existing form of Co species. As shown in Fig. 1c, the adsorption peaks of CdS-O at 2855, 2921 and 2956 cm^{-1} are assigned to C-H stretching vibrations [35]. The peak at 1540 and 1406 cm^{-1} are assigned to the vibration of carboxylate anions [36] and the symmetric stretching vibration of C-O [37], respectively. The band at 721 cm^{-1} is attributed to C-H vibrational mode [35]. According to the FT-IR spectrum of CdS-O, it can be deduced that the ligand of CdS-O is mainly oleic acid. In contrast, the spectrum of CdS-W shows a broad peak at around 3400 cm^{-1}, corresponding to the O-H vibration of MPA. The band at 928 cm^{-1} corresponds to the H-S stretching vibrations of MPA [38]. These results confirm the successful ligand exchange from hydrophobic OA to hydrophilic MPA. Compared to the FT-IR bands of CdS-W, the bands of Co-CdS-W are much weaker, suggesting that a part of the MPA ligands was detached from the surface of CdS-W during photodeposition. For pristine CoS, the peaks at 600 and 1068 cm^{-1} are assigned to the vibration of Co-S bond [39]. However, because of the low CoS content and weak infrared absorption of Co-CdS-W, these peaks are not obvious in the FT-IR spectrum. Raman measurements were employed to further confirm the form of Co species on the CdS surface. As shown in Fig. 1d, the Raman spectrum of CdS-W exhibits two peaks at 295 and 590 cm^{-1}, which are indexed to the first and second harmonic phonons of pure CdS, respectively [40]. As for Co-CdS-W, the two peaks are shifted to 301 and 602 cm^{-1}, respectively, and their intensity decreases dramatically, indicating a strong interaction between CdS and
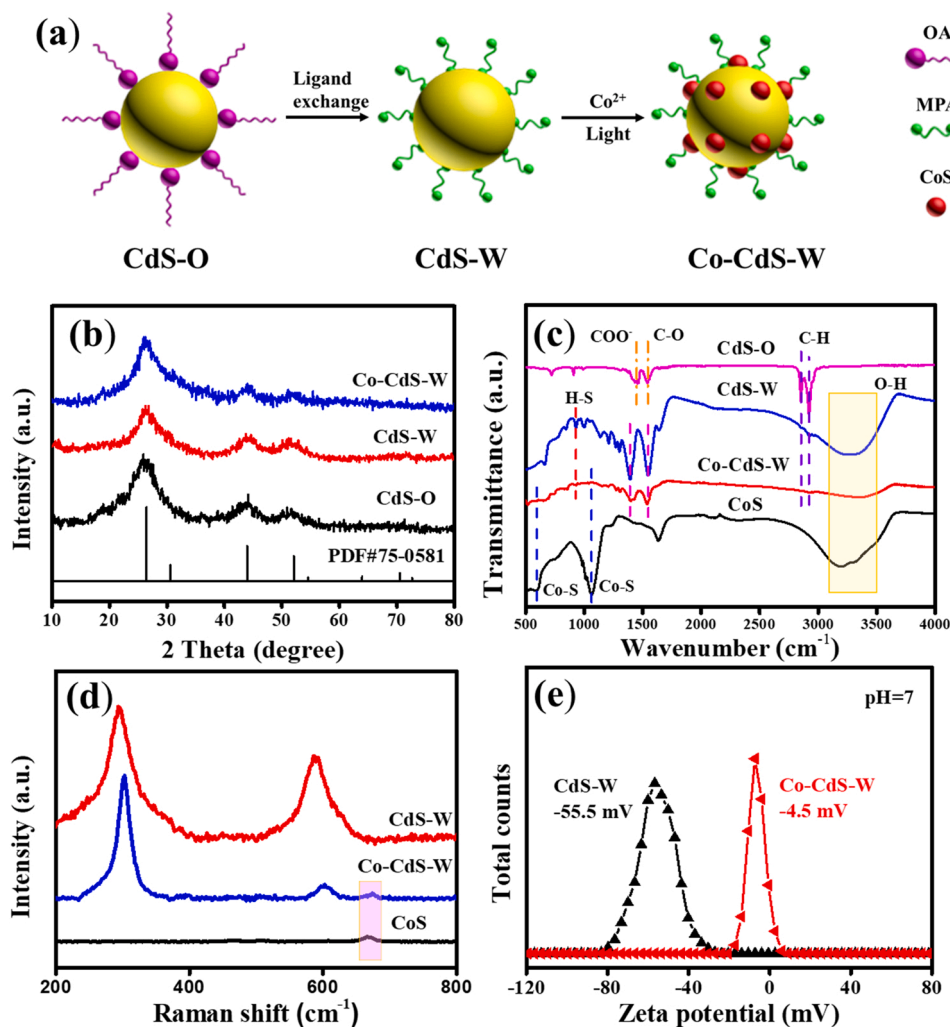
Fig. 1. a) Schematic illustration of ligand exchange and photodeposition methods for the synthesis of Co-CdS-W. b) XRD patterns of CdS-O, CdS-W, and Co-CdS-W. The bottom XRD pattern refers to standard CdS. c) FT-IR spectra of CdS-O, CdS-W, CoS, and Co-CdS-W. d) Raman spectra of CdS-W, Co-CdS-W, and CoS. e) Zeta potential of CdS-W and Co-CdS-W at pH = 7.

Co. A new peak appears at 674 cm^{-1} for Co-CdS-W, indicating the formation of CoS [41]. The strong interaction is also supported by Zeta potential measurements. Since the Zeta potential of CdS-W (Fig. 1e) is -55.5 mV at pH= 7, the positive ions (Co^{2+}) can be easily adsorbed to the surface of CdS-W through electrostatic interaction. The strong interaction between CdS-W and Co^{2+} leads to positively shifted Zeta potential of Co-CdS-W (-4.5 mV).

The morphology and structure of the prepared samples were characterized by transmission electron microscopy (TEM) and high-resolution transmission electron microscopy (HRTEM). As shown in Fig. 2a, the prepared CdS-W presents plenty of quasi-spherical shapes with a diameter of about 4 nm. HRTEM image reveals the highly crystalline structure of CdS-W. The lattice spacing is 0.33 nm, corresponding to the (111) faces of cubic CdS [42]. The TEM and HRTEM images of Co-CdS-W (Fig. 2b) exhibit morphologies similar to those of CdS-W. To explore the dispersion of Co species in Co-CdS-W, energy dispersive X-ray spectrometer (EDS) elemental mappings measurements of Co-CdS-W were performed. As shown in Fig. 2c, Cd, S, and Co elements are all distributed in the selected region, indicating that Co is uniformly dispersed on CdS.

X-ray photoelectron spectroscopy (XPS) measurements were employed to measure surface chemical compositions and chemical states of the elements. The survey spectra (Fig. S1a) suggest the existence of C, Cd, S, and O in CdS-W and Co-CdS-W. The C element is mainly

originated from adventitious hydrocarbons from the XPS instrument and MPA ligands. The O element mainly derives from the carboxyl group of MPA. For CdS-W, the small Na signal indicates the existence of Na$^+$, which was introduced during pH adjustment to balance surface charges. However, the Na$^+$ is replaced by Co^{2+} in Co-CdS-W. As for the Cd 3d spectrum of CdS-W (Fig. S1b), two peaks at 404.8 eV and 411.5 eV can be ascribed to the Cd 3d$_{5/2}$ and Cd 3d$_{3/2}$, respectively [43,44]. The S$_{2p}$ spectrum (Fig. S1c) can be fitted by two peaks at 161.3 eV and 162.7 eV, corresponding to S 2p$_{3/2}$ and 2p$_{1/2}$, respectively [45,46]. Compared with those of CdS-W, the peaks of Cd 3d and S 2p in Co-CdS-W both shift to higher binding energy by 0.4 eV and 0.2 eV, respectively, indicating the transfer of free electrons from CdS to CoS upon their contact [47]. In the Co 2p spectrum of Co-CdS-W (Fig. S1d), two peaks at 781.0 eV and 796.5 eV are ascribed to Co 2p$_{3/2}$ and Co 2p$_{1/2}$, respectively [48]. The other peaks at 786.9 eV and 802.7 eV can be attributed to satellite peaks of Co 2p. These results indicate that Co species is in the form of Co^{2+} [49], consistent with the Raman results suggesting that Co mainly exists as CoS.

The percentage of Cd, S, and Co elements at the surface of CdS-W and Co-CdS-W was estimated from the XPS data listed in Table 1. The CdS-W surface is mainly composed of Cd (51.9%) and S (48.1%). After the integration of Co^{2+}, the percentages of Cd, S, and Co on the surface of Co-CdS-W are 45.5%, 46.7%, and 7.8%, respectively. On the one hand, the Cd-to-S ratio decreases from 1.079 in pure CdS-W to 0.974 in Co-
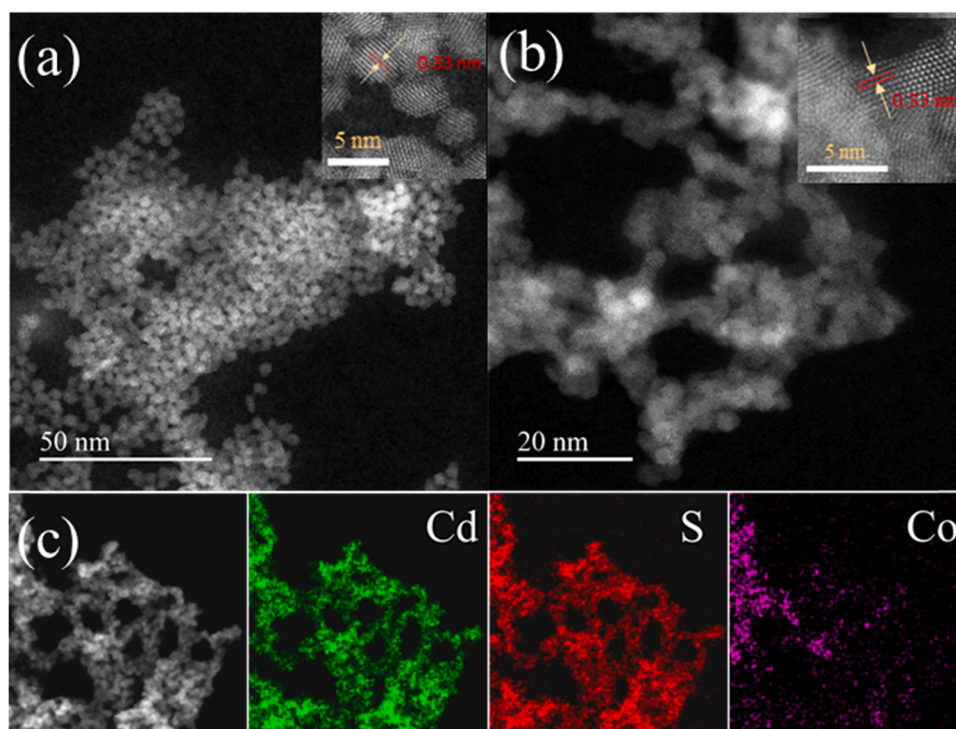
Fig. 2. TEM images of a) CdS-W and b) Co-CdS-W. The inset of are HRTEM images of CdS-W and Co-CdS-W, respectively. c) TEM image and the corresponding EDS elemental mappings of Co-CdS-W.

Table 1
Estimated surface percentage of Cd, S, and Co elements in CdS-W and Co-CdS-W based on XPS data.

Samples	Cd	S	Co	Cd/S	(Cd + Co)/S
CdS-W	51.9%	48.1%	0	1.079	1.08
Co-CdS-W	45.5%	46.7%	7.8%	0.974	1.14

CdS-W. This can be interpreted as that the surface Cd^{2+} ions are partially replaced by Co^{2+} during photodeposition. On the other hand, the increase of (Cd + Co)-to-S ratio from 1.08 in CdS-W to 1.14 in Co-CdS-W suggests that the MPA ligands are partly detached from the surface of CdS QDs [50]. The partial dissociation of MPA ligands from CdS surface will benefit the binding of Co^{2+} to surface S^{2-}.

3.2. Photocatalytic hydrogen production activity

Photocatalytic experiments for H_2 production and organic synthesis were carried out in a 100 mL three-necked flask using a 300 W Xe lamp as the light source. Control experiments (Fig. 3a) showed that no hydrogen was detected either in dark or without photocatalysts, indicating that hydrogen was generated via the photocatalytic process. Pristine CdS-W showed a limited photocatalytic H_2-production rate (72.4 mmol g^{-1} h^{-1}) in the presence of BA, which was attributed to the fast recombination of photogenerated carriers in pristine CdS-W. With the addition of Co^{2+} cocatalysts, the photocatalytic H_2-production activity was enhanced, and the H_2-production rate reached the maximum of 257.8 mmol g^{-1} h^{-1} at a Co^{2+} concentration of 1.6 mM (Fig. 3b), exceeding that of pure CdS-W by 3.6 folds. The corresponding apparent quantum yield is 69.3% under 365 nm light irradiation. There is no significant increment in the H_2-production rates by further increasing Co^{2+} concentrations beyond 1.6 mM. Thus, 1.6 mM is determined as the optimum Co^{2+} concentration. In addition, we recorded the photocatalytic H_2 evolution performance using 10 mg of CdS-W and 8 mM Co^{2+} in 10 mL of water, and the bubbles of evolved H_2 can be clearly

observed (Supporting Information: video).

To prove that selective BA oxidation is a suitable half reaction to be coupled with H_2 production, we conducted photocatalytic measurements with the addition of other alcohols for comparison. In the absence of alcohols, the photocatalytic H_2-production rate was merely 1.7 mmol g^{-1} h^{-1} because photogenerated holes could not be efficiently consumed by the slow OER, leading to hole accumulation and rapid charge carrier recombination. As shown in Fig. 3c, in the presence of different alcohols (methanol, ethanol, 1-butanol, or 1-hexanol), the H_2 yields increase. However, the increment of H_2 yield is the highest when BA was used, indicating that BA is an ideal alcohol to enhance the photocatalytic performance of CdS-W.

To evaluate the effects of CoS cocatalyst in boosting the photoactivity, the H_2-production rates were compared between CdS-W modified by CoS or Platinum (Pt), a common cocatalyst widely used for photocatalytic hydrogen evolution [51–53]. As the reference sample, CdS-W is loaded with 5% Pt by photodeposition of chloroplatinic acid (H_2PtCl_6) onto CdS-W QDs. As shown in Fig. 3d, the H_2-production rate of Pt-modified CdS-W is even lower than that of pure CdS-W. This is probably because the direct loading of the Pt cocatalyst onto QDs is limited by the extremely small size of QDs as well as the complex surface MPA ligands [54].

To investigate the advantages of QDs over nanoparticles (NPs), photocatalytic H_2-production experiments were conducted on CdS NPs with similar crystalline structures (Fig. S2) but larger particle sizes (Fig. S3). The experimental conditions for H_2 production are listed in Table S2. The amounts of products (H_2, BD, and benzoic acid (BAC)) over CdS NPs, Co-CdS NPs, CdS-W QDs, and Co-CdS-W QDs are shown in Fig. 3e. After irradiation for 1 h, the amount of H_2 production over CdS NPs is 0.022 mmol, much lower than that of CdS-W (0.15 mmol). This is attributed to the small particle size of CdS QDs, which exposes more surface active sites and shortens the carrier transfer distance to these sites. After coupling with Co^{2+}, H_2 yields over Co-CdS NPs and Co-CdS-W increase to 0.048 mmol and 0.58 mmol, respectively, suggesting that Co^{2+} is a suitable cocatalyst for both CdS NPs and CdS-W. Moreover, both CdS-W and Co-CdS-W QDs present relatively low amounts of BAC
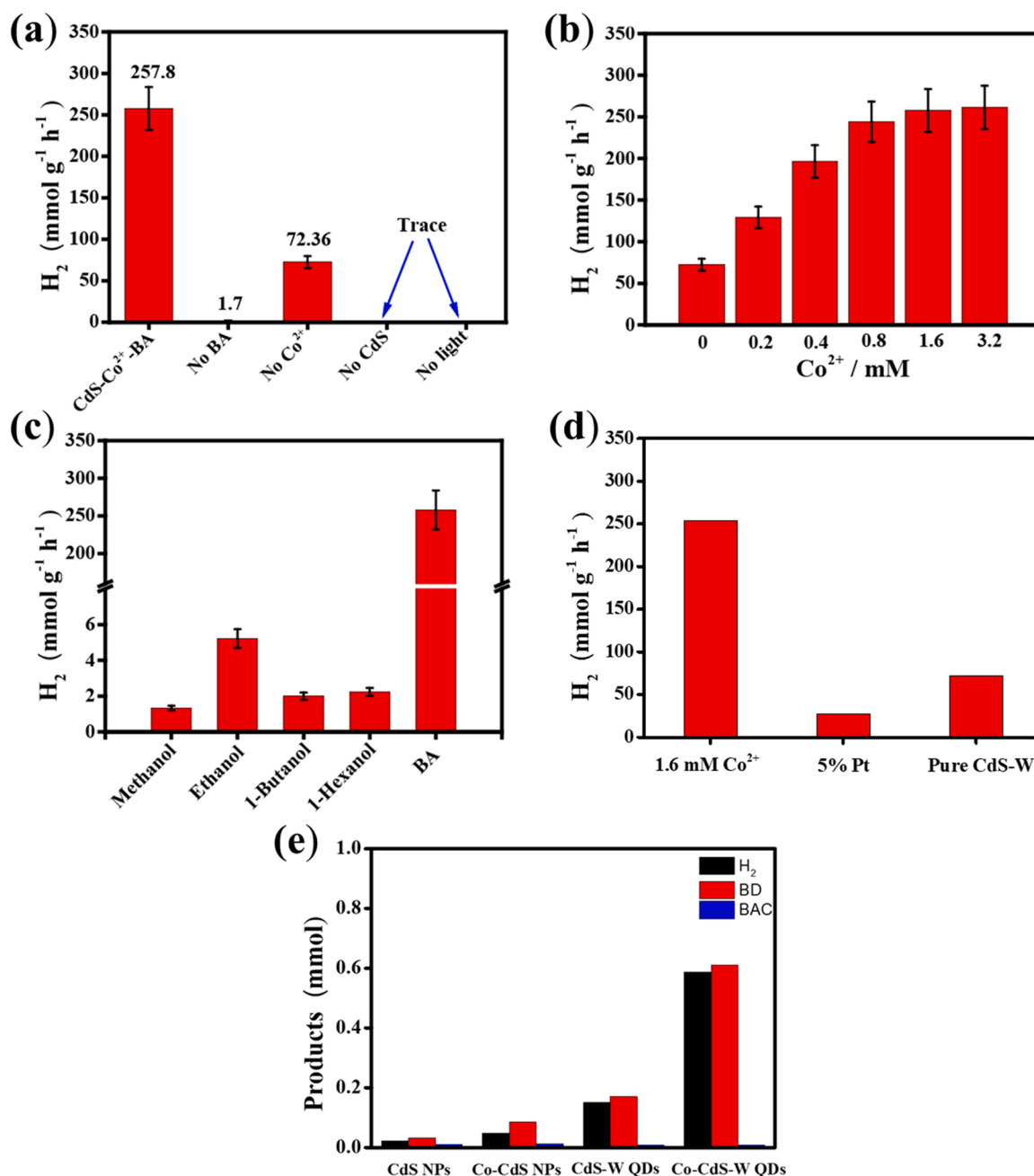
Fig. 3. Photocatalytic H_2-production activity of the prepared samples under different conditions: a) control experiments, b) adding different concentrations of $CoCl_2 \cdot 6H_2O$, c) in the presence of different alcohols, d) adding Co^{2+} or Pt cocatalysts. e) The amounts of H_2, BD, and BAC products over CdS NPs, Co-CdS-W NPs, CdS-W QDs, and Co-CdS-W QDs in 80 mL of BA aqueous solution (20 mM) under light irradiation for 1 h.

compared to that of BD and H_2, suggesting excellent BD selectivity.

To further study the kinetics and selectivity of the oxidation half reactions, high-performance liquid chromatography (HPLC) was applied to monitor the changes in the concentrations of BA and oxidation products. Meanwhile, gas chromatography was applied to detect the amount of evolved H_2. The photocatalytic measurements were performed in a solution containing 2 mg of CdS-W, 0.128 mmol of Co^{2+}, 1.6 mmol of BA, and 80 mL of deionized water using the photocatalyst (Co-CdS-W). As shown in Fig. 4, the initial amount of BA (1.49 mmol) is lower than the added amount (1.60 mmol) due to the adsorption of BA to the surface of CdS QDs. With the progression of photoreactions, the amount of BA decreases rapidly, while the amounts of BD and H_2 increase. In this photocatalytic system, H_2 evolution and BA oxidation to BD are both two-electron processes. The ratio of BD to H_2 yields is

approximately 1:1, indicating that both the photogenerated electrons and holes are fully utilized for hydrogen production and selective BA oxidation, respectively. Notably, the BAC yield is negligible, indicating high selectivity of BA oxidation to BD. The conversion and BD selectivity reach 27.3% and 83.4% after reaction for 30 min, respectively, and further reach 83.9% and 77.6% after 3 h, respectively. The BA conversion over the prepared Co-CdS-W can be fitted by pseudo-first-order kinetics, and the fit parameters are listed in Fig. S4.

H NMR measurements were employed to identify the photocatalytic products. Fig. S5 and S6 are the standard H NMR spectra of BA and BD, respectively. Fig. S7 presents the H NMR spectrum of the reaction liquid after the photocatalytic process for 3 h. Both BA and BD are detected while BAC is absent, indicating high selectivity of BA oxidation to BD.

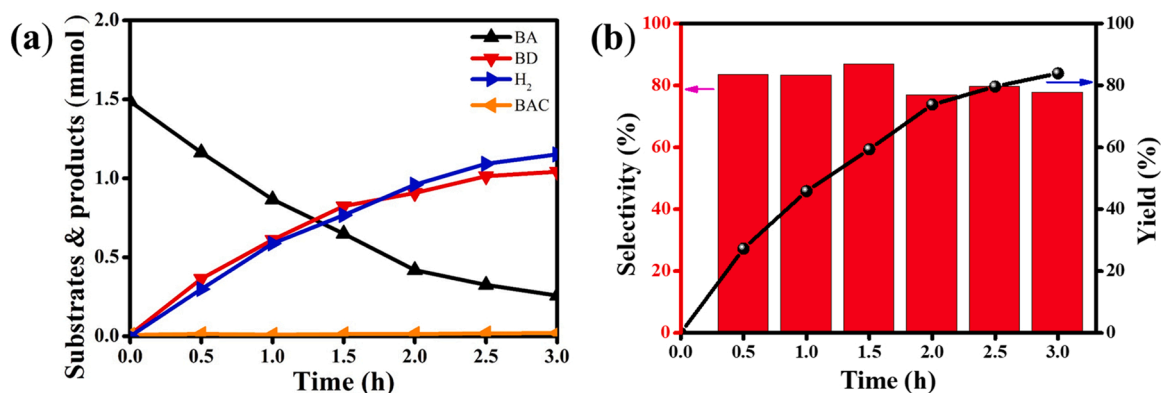To investigate the stability of the photocatalyst, cycle tests were

Fig. 4. a) The time course of hydrogen, BA, BD, and BAC evolution on Co-CdS-W; b) The time course of the selectivity and yield of BD on Co-CdS-W.

performed. As shown in Fig. S8, the photocatalytic performance is slightly reduced, which may be attributed to the loss of photocatalyst during recycles. The morphology of Co-CdS-W shows no obvious change after photocatalysis (Fig. S9). In addition, the XRD (Fig. S10a) and XPS (Fig. S10b,c,d) spectra of Co-CdS-W after photocatalytic reaction show inappreciable change compared with the fresh sample, which prove the structural stability of Co-CdS-W.

3.3. Reaction mechanism

Generally, photocatalytic H_2-production involves three steps: light absorption, photogenerated carrier separation, and surface photocatalytic reactions.

To investigate the light absorption properties of the samples, ultraviolet-visible (UV–vis) absorption spectroscopy was conducted. As shown in Fig. S11a, pristine CdS-W shows an obvious absorption edge around 451 nm, corresponding to a band gap of 2.75 eV for CdS-W. Compared with CdS-W, Co-CdS-W shows an expanded absorption of visible and near-infrared lights, which is due to the *d-d* transition of Co (II) and light absorption by the black CoS [55]. In addition, there is no obvious difference between the absorption edges of Co-CdS-W and CdS-W, implying that the properties of CdS are not altered by the addition of CoS.

Steady-state photoluminescence (PL) spectroscopy (Fig. S11b) and time-resolved photoluminescence (TRPL) spectroscopy (Fig. S11c) were used to assess the separation efficiency of photogenerated carriers. As shown in Fig. S11b, two peaks at 471 and 607 nm in the PL spectrum of CdS-W are ascribed to the band edge emission and trap emission of CdS, respectively [50]. Compared to CdS-W, Co-CdS-W presents a much lower PL intensity, indicating suppressed photogenerated carrier recombination. In the TRPL spectra, the decay curves in Fig. S11c are fitted by a double-exponential equation. The short lifetime (τ_1) and the long lifetime (τ_2) can be attributed to the radiative decay and non-radiative decay processes, respectively. The τ_1 and τ_2 of Co-CdS-W are both lower than those of CdS-W. Plus, Co-CdS-W presents a much lower average lifetime than CdS-W, indicating enhanced transfer efficiency of photogenerated carriers.

Femtosecond transient absorption (fs-TA) spectroscopy was used to further explore the transfer efficiency of photogenerated carriers and the roles of CoS in boosting the photocatalytic activity of CdS-W. Fig. 5a-e presents the fs-TA spectra of CdS-W and Co-CdS-W. The negative and positive ΔOD signals are assigned to the photobleaching (PB) and photoinduced absorption (PA) signals, respectively [56]. Due to the high degeneracy of hole levels and high effective mass of the holes, the PB signals mainly reflect the quenching of photogenerated electrons [57]. The spectra of CdS-W (Fig. 5c) present negative PB signals within the wavelength range of 450–540 nm. Furthermore, broad positive PA signals at the wavelength of 550–700 nm are observed, corresponding to the traped holes in CdS [58]. The spectra of Co-CdS-W (Fig. 5d) show PB

signals similar to those of CdS. However, the PA signals are absent in the range of 550–700 nm for Co-CdS-W, indicating that there is no significant amount of trapped holes in Co-CdS-W [59]. This result reveals the role of CoS as a hole transfer cocatalyst. Once the CdS are photoexcited, photogenerated holes rapidly transfer from CdS to CoS for the oxidation of BA, and the photogenerated electrons in CdS are used for H_2 production. Since the PB signals reflect the electron transfer dynamics of CdS, we traced the kinetic at 470 nm for CdS-W and Co-CdS-W (Fig. 5e). The amplitude-weighted electron transfer time of CdS and Co-CdS-W is calculated to be 30.51 ps and 44.33 ps (see Table 2), respectively. For Co-CdS-W, because the trapped holes rapidly transfer from CdS to CoS, the electron-hole recombination in CdS is suppressed. Thus, Co-CdS-W shows an extended lifetime for photogenerated electrons. This result supports the conclusion that CoS serves as a hole transfer cocatalyst.

Mott–Schottky (M-S) measurements were used to evaluate the semiconductor type of CdS-W and its flat band potential. As shown in Fig. S12, the M-S curves of CdS-W present positive slopes, indicating that CdS-W is an n-type semiconductor. The conduction band (CB) position of the n-type semiconductor is − 0.1 V more negative than the flat band position [34]. Thus, the CB position of CdS-W is − 1.10 V (vs normal hydrogen electrode, NHE). Combined with the band gap of CdS-W (2.75 eV), the valence band (VB) position of CdS-W is calculated to be + 1.65 V. According to reported values, the redox potential of BA/BD is 0.68 V(vs NHE) [60], and the redox potential of H_2O/O_2 is 1.23 V (vs NHE). Thus, upon light irradiation, the photogenerated holes tend to oxidize BA to BD more than H_2O to O_2 (Fig. 5f). The BD products cannot be further oxidized to BAC because the redox potential of BD/BAC (+2.5 V vs NHE) is more positive than the VB position of CdS-W [61]. Thus, high BD selectivity is achieved.

To investigate the reaction mechanism for H_2 evolution, the photocatalytic measurements were conducted in isotope-labeled D_2O solution, and the gaseous products were detected by chromatograph-mass spectroscopy (GC–MS). As shown in Fig. S13, the *m/z* signals at 2, 3, 4, 18, and 40 are indexed to H_2, HD, D_2, D_2O, and Ar, respectively. D_2 (*m/z* = 4) was detected as the main product with a trace amount of HD (*m/z* = 3). The HD signal arises from the reduction of H^+ and D^+ from the aqueous solution, where the H^+ is originated from the oxidation of BA to BD.

Density functional theory (DFT) calculations were used to further investigate the reaction pathway of BA oxidation on Co-CdS-W. The pathway consists of two consecutive dehydrogenation steps. As shown in Fig. 6a, the first dehydrogenation step leads to the formation of a carbon-centered radical or an oxygen-centered radical. The energy barrier for the carbon-centered radical is lower than that for the oxygen-centered radical, suggesting that the H atom in C-H bond is dissociated first, followed by the breakage of O-H bond to form BD. On Co-CdS-W, the rate-limiting step is the activation of the C-H (0.51 eV, Fig. 6b). On CdS-W, however, this step is spontaneous (−0.65 eV, Fig. S14), and the rate-limiting step becomes the activation of O-H (1.44 eV). Overall,
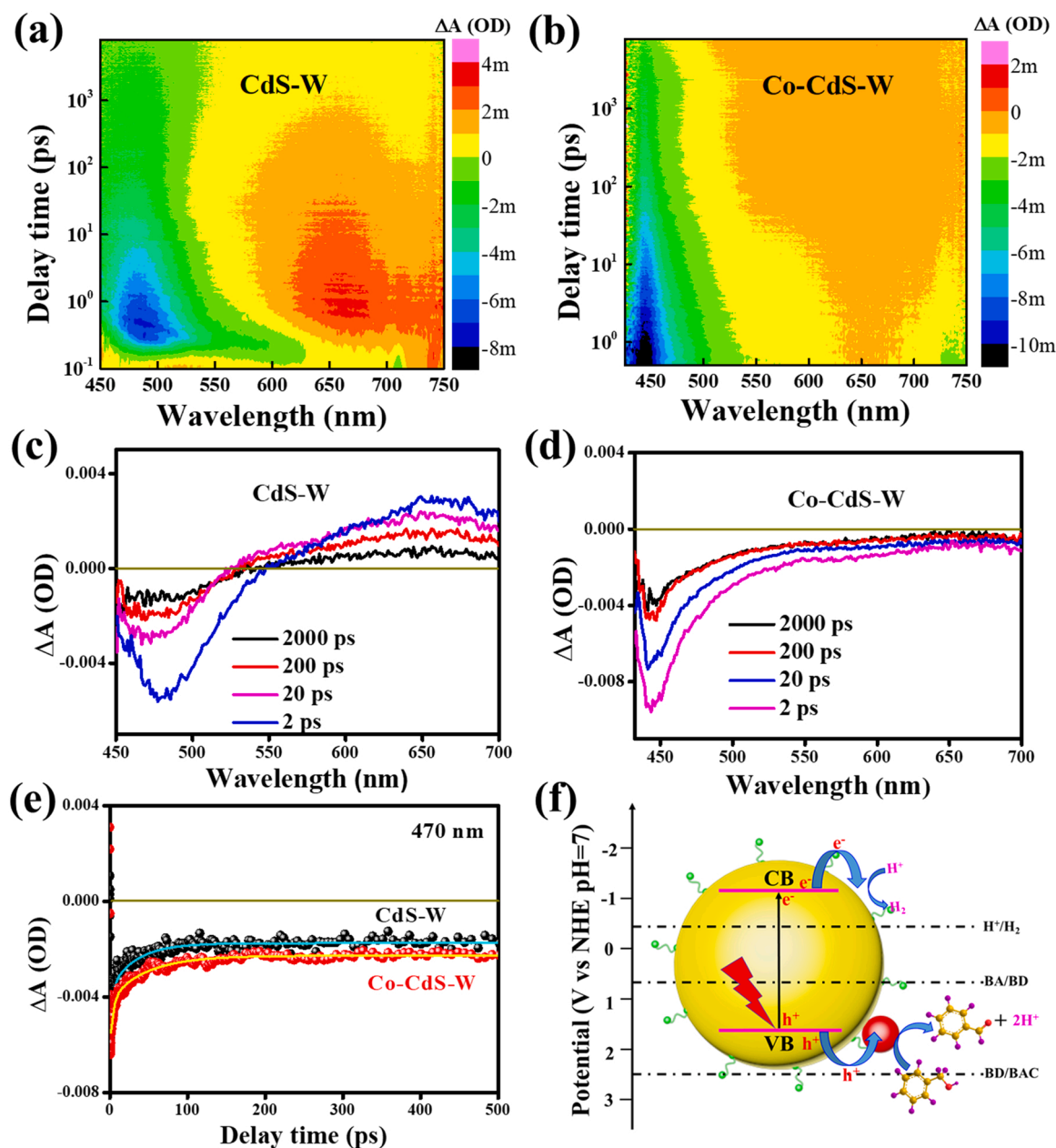
Fig. 5. Pseudo-color transient absorption plot of a) CdS-W and b) Co-CdS-W. fs-TA spectra of c) CdS-W and d) Co-CdS-W at indicated delay times, and e) the corresponding decay curves of the signals at 470 nm for CdS-W and Co-CdS-W. f) Schematic illustration for photocatalytic hydrogen production coupled with BA oxidation over Co-CdS-W.

Table 2
Fitting parameters of fs-TA kinetics trace of CdS-W and Co-CdS-W at 470 nm.

Sample	τ_1 (/ps)	A_1	τ_2 (/ps)	A_2	τ_a (/ps)
CdS-W	2.71	0.90	33.69	0.10	30.51
Co-CdS-W	4.05	0.07	47.41	0.93	44.33

the activation barrier for BA oxidation is much higher on CdS-W than that on Co-CdS-W, and thus the dehydrogenization process on Co-CdS-W is kinetically much more feasible than that on CdS-W.

Based on the results and discussion above, a possible mechanism is speculated in Fig. 6c. Initially, BA is adsorbed on the surface of Co-CdS-W. Upon light irradiation, electrons in CdS are photoexcited from its VB to CB, leaving the holes in the VB. The photogenerated electrons are used to reduce H^+ to H_2. Meanwhile, the holes transfer to the CoS

cocatalysts to oxidize adsorbed BA to BD via two consecutive steps. In the first step, a BA molecule combines with a hole to form a H^+ and a carbon-centered radical. Subsequently, another hole further oxidizes the intermediate to BD while releasing another H^+. The BD then desorbs as the final product. The H^+ ions are released into the water and can be reduced for H_2 production.

4. Conclusions

In conclusion, Co-modified CdS QDs were successfully prepared via a simple solvothermal method followed by ligand exchange and photo-deposition of Co^{2+}. The samples show excellent performance towards photocatalytic H_2 evolution and selective BA oxidation to BD. The fs-TA spectra show that CoS serves as a hole cocatalyst to extract photo-generated holes from BD, facilitating the separation of photogenerated carriers. Besides, CoS enhances visible light absorption due to its black
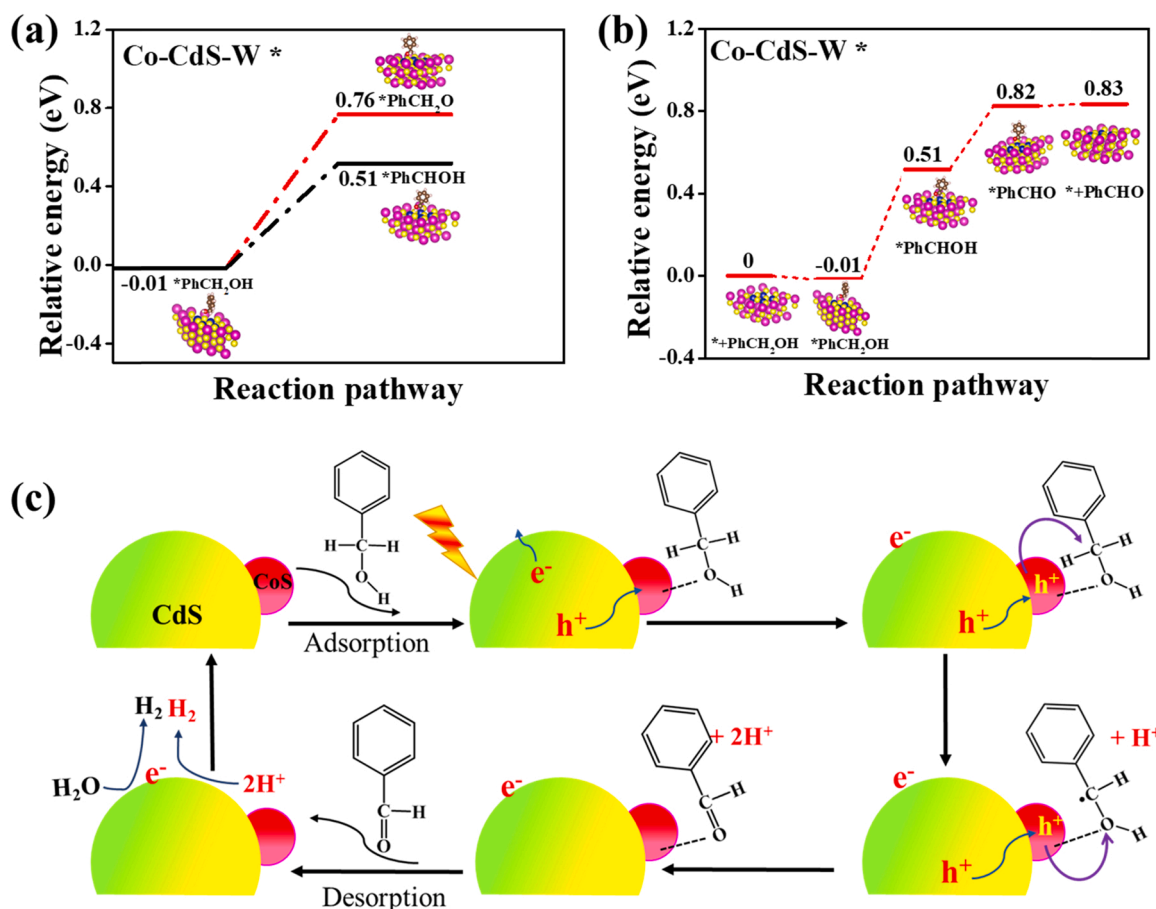
Fig. 6. a) DFT-calculated energy barriers for BD oxidation to different intermediates on Co-CdS-W; b) DFT-calculated energy diagram of BA oxidation to BD on Co-CdS-W; c) Speculated mechanism of photocatalytic H_2 production coupled with selective BA oxidation to BD over Co-CdS-W.

color and the *d-d* transition of Co(II). Therefore, a high H_2-production activity and high BD productivity are achieved. High BD selectivity is achieved because the photocatalytic system lacks the driving force to further oxidize BD to BAC. DFT result reveals a much lower activation barrier for BA oxidation to BD on Co-CdS-W than that on CdS-W, providing theoretical support for the superior photoactivity of Co-CdS-W. This work will shed light on the design of photocatalytic systems with efficient H_2 production and the synthesis of valuable organic compounds.

CRediT authorship contribution statement

Xianglin Xiang: Methodology, Data curation, Writing – original draft. **Bicheng Zhu:** Software, Formal analysis. **Jianjun Zhang:** Investigation, Data curation. **Chenhui Jiang:** Investigation, Resources. **Tao Chen:** Investigation, Resources. **Huogen Yu:** Supervision. **Jiaguo Yu:** Project administration, Funding acquisition. **Linxi Wang:** Conceptualization, Supervision, Writing – review & editing.

Declaration of Competing Interest

The authors declare that they have no known competing financial interests or personal relationships that could have appeared to influence the work reported in this paper.

Data availability

Data will be made available on request.

Acknowledgments

Appendix A. Supplementary material

Supplementary data associated with this article can be found in the online version at doi:10.1016/j.apcatb.2022.122301.

References

[1] S. Wageh, A.A. Al-Ghamdi, O.A. Al-Hartomy, M.F. Alotaibi, L. Wang, CdS/polymer S-scheme H_2-production photocatalyst and its in-situ irradiated electron transfer mechanism, Chin. J. Catal. 43 (2022) 586–588.

[2] M. Sayed, J. Yu, G. Liu, M. Jaroniec, Non-noble plasmonic metal-based photocatalysts, Chem. Rev. 122 (2022) 10484–10537.

[3] E. Zhang, Q. Zhu, J. Huang, J. Liu, G. Tan, C. Sun, T. Li, S. Liu, Y. Li, H. Wang, X. Wan, Z. Wen, F. Fan, J. Zhang, K. Ariga, Visually resolving the direct Z-scheme heterojunction in CdS@ZnIn2S4 hollow cubes for photocatalytic evolution of H2 and H2O2 from pure water, Appl. Catal. B 293 (2021), 120213.

[4] C. Bie, L. Wang, J. Yu, Challenges for photocatalytic overall water splitting, Chem 8 (2022) 1567–1574.

[5] M.Z. Rahman, T. Edvinsson, J. Gascon, Hole utilization in solar hydrogen production, Nat. Rev. Chem. 6 (2022) 243–258.

[6] M. Liu, W. You, Z. Lei, T. Takata, K. Domen, C. Li, Photocatalytic water splitting to hydrogen over a visible light-driven LaTaON$_2$ catalyst, Chin. J. Catal. 27 (2006) 556–558.

[7] C. Cheng, B. He, J. Fan, B. Cheng, S. Cao, J. Yu, An inorganic/organic S-scheme heterojunction H_2-production photocatalyst and its charge transfer mechanism, Adv. Mater. 33 (2021) 2100317.

[8] J.J. Wang, Z.J. Li, X.B. Li, X.B. Fan, Q.Y. Meng, S. Yu, C.B. Li, J.X. Li, C.H. Tung, L. Z. Wu, Photocatalytic hydrogen evolution from glycerol and water over nickel-hybrid cadmium sulfide quantum dots under visible-light irradiation, ChemSusChem 7 (2014) 1468–1475.

[9] T. Di, L. Zhang, B. Cheng, J. Yu, J. Fan, CdS nanosheets decorated with Ni@ graphene core-shell cocatalyst for superior photocatalytic H2 production, J. Mater. Sci. Technol. 56 (2020) 170–178.

[10] J.C. Colmenares, W.Y. Ouyang, M. Ojeda, E. Kuna, O. Chernyayeva, D. Lisovytskiy, S. De, R. Luque, A.M. Balu, Mild ultrasound-assisted synthesis of TiO2 supported on magnetic nanocomposites for selective photo-oxidation of benzyl alcohol, Appl. Catal. B 183 (2016) 107–112.

[11] A. Maldotti, A. Molinari, R. Amadelli, Photocatalysis with organized systems for the oxofunctionalization of hydrocarbons by O2, Chem. Rev. 102 (2002) 3811–3836.

[12] Z. Zheng, F. Han, B. Xing, X. Han, B. Li, Synthesis of Fe3O4@CdS@CQDs ternary core–shell heterostructures as a magnetically recoverable photocatalyst for selective alcohol oxidation coupled with H2O2 production, J. Colloid Interface Sci. 624 (2022) 460–470.

[13] B. Zhan, M.A. White, T. Sham, J.A. Pincock, R.J. Doucet, K.V.R. Rao, K. N. Robertson, T.S. Cameron, Zeolite-confined nano-RuO2: a green, selective, and efficient catalyst for aerobic alcohol oxidation, J. Am. Chem. Soc. 125 (2003) 2195–2199.

[14] S.R. Joshi, K.L. Kataria, S.B. Sawant, J.B. Joshi, Kinetics of oxidation of benzyl alcohol with dilute nitric acid, Ind. Eng. Chem. Res. 44 (2005) 325–333.

[15] C.-C. Guo, Q. Liu, X.-T. Wang, H.-Y. Hu, Selective liquid phase oxidation of toluene with air, Appl. Catal. A Gen. 282 (2005) 55–59.

[16] T. Mallat, A. Baiker, Oxidation of alcohols with molecular oxygen on solid catalysts, Chem. Rev. 104 (2004) 3037–3058.

[17] B. Xia, Y. Zhang, B. Shi, J. Ran, K. Davey, S. Qiao, Photocatalysts for hydrogen evolution coupled with production of value-added chemicals, Small Methods 4 (2020) 2000063.

[18] Q. Yang, T. Wang, Z. Zheng, B. Xing, C. Li, B. Li, Constructing interfacial active sites in Ru/g-C3N4−x photocatalyst for boosting H2 evolution coupled with selective benzyl-alcohol oxidation, Appl. Catal. B 315 (2022), 121575.

[19] X. Li, T. Wang, Z. Zheng, Q. Yang, C. Li, B. Li, Pd modified defective HNb3O8 with dual active sites for photocatalytic coproduction of hydrogen fuel and value-added chemicals, Appl. Catal. B 296 (2021), 120381.

[20] X. Xiang, L. Wang, J. Zhang, B. Cheng, J. Yu, W. Macyk, Cadmium chalcogenide (CdS, CdSe, CdTe) quantum dots for solar-to-fuel conversion, Adv. Photonics Res. 3 (2022) 2200065.

[21] H. Wu, X. Li, C. Tung, L. Wu, Semiconductor quantum dots: an emerging candidate for CO2 photoreduction, Adv. Mater. 31 (2019) 1900709.

[22] X. Li, C. Tung, L. Wu, Semiconducting quantum dots for artificial photosynthesis, Nat. Rev. Chem. 2 (2018) 160–173.

[23] D. Gao, J. Xu, L. Wang, B. Zhu, H. Yu, J. Yu, Optimizing atomic hydrogen desorption of sulfur-rich NiS1+x cocatalyst for boosting photocatalytic H2 evolution, Adv. Mater. 34 (2022) 2108475.

[24] Y. Xia, M. Sayed, L. Zhang, B. Cheng, J. Yu, Single-atom heterogeneous photocatalysts, Chem. Catal. 1 (2021) 1173–1214.

[25] J. Liu, J. Feng, J. Gui, T. Chen, M. Xu, H. Wang, H. Dong, H. Chen, X. Li, L. Wang, Z. Chen, Z. Yang, J. Liu, W. Hao, Y. Yao, L. Gu, Y. Weng, Y. Huang, X. Duan, J. Zhang, Y. Li, Metal@semiconductor core-shell nanocrystals with atomically organized interfaces for efficient hot electron-mediated photocatalysis, Nano Energy 48 (2018) 44–52.

[26] Z.J. Li, J.J. Wang, X.B. Li, X.B. Fan, Q.Y. Meng, K. Feng, B. Chen, C.H. Tung, L. Z. Wu, An exceptional artificial photocatalyst, Nih-CdSe/CdS core/shell hybrid, made in situ from CdSe quantum dots and nickel salts for efficient hydrogen evolution, Adv. Mater. 25 (2013) 6613–6618.

[27] C. Bie, B. Zhu, L. Wang, H. Yu, C. Jiang, T. Chen, J. Yu, A. Bifunctional, CdS/MoO2/ MoS2 catalyst enhances photocatalytic H2 evolution and pyruvic acid synthesis, Angew. Chem. Int. Ed. 61 (2022), e202212045.

[28] X.B. Li, Y.J. Gao, H.L. Wu, Y. Wang, Q. Guo, M.Y. Huang, B. Chen, C.H. Tung, L. Z. Wu, Assembling metallic 1T-MoS2 nanosheets with inorganic-ligand stabilized quantum dots for exceptional solar hydrogen evolution, Chem. Commun. 53 (2017) 5606–5609.

[29] Q. Quo, F. Liang, X.Y. Gao, Q.C. Gan, X.B. Li, J. Li, Z.S. Lin, C.H. Tung, L.Z. Wu, Metallic Co2C: a promising co-catalyst to boost photocatalytic hydrogen evolution of colloidal quantum dots, ACS Catal. 8 (2018) 5890–5895.

[30] Y. Shang, T. Wang, Y. Xiao, Z. Dong, X. Li, B. Li, Constructing BiOBr/CoOx/g-C3N4 Z-scheme photocatalyst with CoOx as both redox mediator and cocatalyst for phenol degradation, J. Alloy. Compd. 875 (2021), 159998.

[31] M. Sayed, F. Xu, P. Kuang, J. Low, S. Wang, L. Zhang, J. Yu, Sustained CO2-photoreduction activity and high selectivity over Mn, C-codoped ZnO core-triple shell hollow spheres, Nat. Commun. 12 (2021) 4936.

[32] S. Jiao, J. Wang, Q. Shen, Y. Li, X. Zhong, Surface engineering of PbS quantum dot sensitized solar cells with a conversion efficiency exceeding 7%, J. Mater. Chem. A 4 (2016) 7214–7221.

[33] Z. Fang, Y. Wang, J. Song, Y. Sun, J. Zhou, R. Xu, H. Duan, Immobilizing CdS quantum dots and dendritic Pt nanocrystals on thiolated graphene nanosheets toward highly efficient photocatalytic H2 evolution, Nanoscale 5 (2013) 9830–9838.

[34] X. Xiang, B. Zhu, B. Cheng, J. Yu, H. Lv, Enhanced photocatalytic H2-production activity of CdS quantum dots using Sn2+ as cocatalyst under visible light irradiation, Small 16 (2020) 2001024.

[35] N.A. Hamizi, M.R. Johan, Z.Z. Chowdhury, Y.A. Wahab, Y. Al-Douri, A.M. Saat, O. A. Pivehzhani, Raman spectroscopy and FTIR spectroscopy studies of Mn-doped CdSe QDs at different particles size, Optik 179 (2019) 628–631.

[36] X. Huang, Y. Chen, X. Feng, X. Hu, Y. Zhang, L. Liu, Incorporation of oleic acid-modified Ag@ZnO core-shell nanoparticles into thin film composite membranes for enhanced antifouling and antibacterial properties, J. Membr. Sci. 602 (2020), 117956.

[37] M.N. Kalasad, A.K. Rabinal, B.G. Mulimani, Ambient synthesis and characterization of high-quality cdse quantum dots by an aqueous route, Langmuir 25 (2009) 12729–12735.

[38] P. Sheng, W. Li, J. Cai, X. Wang, X. Tong, Q. Cai, C. Grimes, A novel method for the preparation of a photocorrosion stable core/shell CdTe/CdS quantum dot TiO2 nanotube array photoelectrode demonstrating an AM 1.5G photoconversion efficiency of 6.12%, J. Mater. Chem. A 1 (2013) 7806–7815.

[39] H. He, Efficient interface-induced effect of novel reduced graphene oxide-CoS heteronanostructures in enhancing photocatalytic acitivties, Appl. Surf. Sci. 421 (2017) 260–267.

[40] N. Li, Y. Ding, J. Wu, Z. Zhao, X. Li, Y. Zheng, M. Huang, X. Tao, Efficient, full spectrum-driven H2 evolution Z-scheme Co2P/CdS photocatalysts with Co-S bonds, ACS Appl. Mater. Interfaces 11 (2019) 22297–22306.

[41] A.S. Pawar, S.S. Garje, Synthesis of Co9S8 and CoS nanocrystallites using Co(II) thiosemicarbazone complexes as single-source precursors, Bull. Mater. Sci. 38 (2015) 1843–1850.

[42] J. Guo, Y. Cao, R. Shi, G.I.N. Waterhouse, L. Wu, C. Tung, T. Zhang, A photochemical route towards metal sulfide nanosheets from layered metal thiolate complexes, Angew. Chem. Int. Ed. 58 (2019) 8443–8447.

[43] Z. Jiang, Q. Chen, Q. Zheng, R. Shen, P. Zhang, X. Li, Constructing 1D/2D Schottky-based heterojunctions between Mn0.2Cd0.8S nanorods and Ti3C2 nanosheets for boosted photocatalytic H2 evolution, Acta Phys. Chim. Sin. 37 (2021) 2010059.

[44] C. Ding, C.X. Zhao, S. Cheng, X.F. Yang, Ultrahigh photocatalytic hydrogen evolution performance of coupled 1D CdS/1T-phase dominated 2D WS2 nanoheterojunctions, Chin. J. Catal. 43 (2022) 403–409.

[45] J. Zhang, L. Zhang, W. Wang, J. Yu, In situ irradiated X-ray photoelectron spectroscopy investigation on electron transfer mechanism in S-scheme photocatalyst, J. Phys. Chem. Lett. 13 (2022) 8462–8469.

[46] L. Sun, L.L. Li, J. Yang, J.J. Fan, Q.L. Xu, Fabricating covalent organic framework/ CdS S-scheme heterojunctions for improved solar hydrogen generation, Chin. J. Catal. 43 (2022) 350–358.

[47] B. Zeng, S. Wang, Y. Gao, G. Li, W. Tian, J. Meeprasert, H. Li, H. Xie, F. Fan, R. Li, C. Li, Interfacial modulation with aluminum oxide for efficient plasmon-induced water oxidation, Adv. Funct. Mater. 31 (2021) 2005688.

[48] Z.L. Jin, H.Y. Li, J.K. Li, Efficient photocatalytic hydrogen evolution over graphdiyne boosted with a cobalt sulfide formed S-scheme heterojunction, Chin. J. Catal. 43 (2022) 303–315.

[49] H. Yang, D. Yang, X. Wang, POM-incorporated CoO nanowires for enhanced photocatalytic syngas production from CO2, Angew. Chem. Int. Ed. 59 (2020) 15527–15531.

[50] Z. Li, J. Wang, X. Li, X. Fan, Q. Meng, K. Feng, B. Chen, C. Tung, L. Wu, An exceptional artificial photocatalyst, Nih-CdSe/CdScore/shell hybrid, made in situ from CdSe quantum dots and nickel salts for efficient hydrogen evolution, Adv. Mater. 25 (2013) 6613–6618.

[51] Z. Zhang, L. Wang, B. Cheng, H. Yu, J. Yu, Photocatalytic H2 evolution coupled with furfuralcohol oxidation over Pt-modified ZnCdS solid solution, Small Methods 5 (2021) 2100979.

[52] Y.W. Chen, L.L. Li, Q.L. Xu, T. Duren, J.J. Fan, D.K. Ma, Controllable synthesis of g-C3N4 inverse opal photocatalysts for superior hydrogen evolution, Acta Phys. Chim. Sin. 37 (2021) 2009080.

[53] P. Kuang, Y. Wang, B. Zhu, F. Xia, C. Tung, J. Wu, H. Chen, J. Yu, Pt single atoms supported on N-doped mesoporous hollow carbon spheres with enhanced electrocatalytic H2-evolution activity, Adv. Mater. 33 (2021) 2008599.

[54] X.-B. Li, Y.-J. Gao, Y. Wang, F. Zhan, X.-Y. Zhang, Q.-Y. Kong, N.-J. Zhao, Q. Guo, H.-L. Wu, Z.-J. Li, Y. Tao, J.-P. Zhang, B. Chen, C.-H. Tung, L.-Z. Wu, Self-assembled framework enhances electronic communication of ultrasmall-sized nanoparticles for exceptional solar hydrogen evolution, J. Am. Chem. Soc. 139 (2017) 4789–4796.

[55] K. Li, Y. Lin, K. Wang, Y. Wang, Y. Zhang, Y. Zhang, F. Liu, Rational design of cocatalyst system for improving the photocatalytic hydrogen evolution activity of graphite carbon nitride, Appl. Catal. B 268 (2020), 118402.

[56] J. Zhang, L. Wang, C. Jiang, B. Cheng, T. Chen, J. Yu, CsPbBr3 nanocrystal induced bilateral interface modification for efficient planar perovskite solar cells, Adv. Sci. 8 (2021) 2102648.

[57] J. Zhang, G. Yang, B. He, B. Cheng, Y. Li, G. Liang, L. Wang, Electron transfer kinetics in CdS/Pt heterojunction photocatalyst during water splitting, Chin. J. Catal. 43 (2022) 2530–2538.

[58] K. Wu, H. Zhu, Z. Liu, W. Rodriguez-Cordoba, T. Lian, Ultrafast charge separation and long-lived charge separated state in photocatalytic CdS-Pt nanorod heterostructures, J. Am. Chem. Soc. 134 (2012) 10337–10340.

[59] C.M. Wolff, P.D. Frischmann, M. Schulze, B.J. Bohn, R. Wein, P. Livadas, M. T. Carlson, F. Jackel, J. Feldmann, F. Wurthner, J.K. Stolarczyk, All-in-one visible-

light-driven water splitting by combining nanoparticulate and molecular co-catalysts on CdS nanorods, Nat. Energy 3 (2018) 862–869.

[60] X. Ye, Y. Chen, Y. Wu, X. Zhang, X. Wang, S. Chen, Constructing a system for effective utilization of photogenerated electrons and holes: photocatalytic selective transformation of aromatic alcohols to aromatic aldehydes and hydrogen evolution over $Zn_3In_2S_6$ photocatalysts, Appl. Catal. B 242 (2019) 302–311.

[61] X. Xiao, J. Jiang, L. Zhang, Selective oxidation of benzyl alcohol into benzaldehyde over semiconductors under visible light: the case of $Bi_{12}O_{17}Cl_2$ nanobelts, Appl. Catal. B 142–143 (2013) 487–493.